

Densities and temperatures in the Venus mesosphere and lower thermosphere retrieved from SOIR on board Venus Express.

Part I. Retrieval technique

A. Mahieux,^{*,1} A.C. Vandaele,¹ E. Neefs,¹ S. Robert,¹ V. Wilquet,¹ R. Drummond,¹

A. Federova² and J.L. Bertaux^{3,4}

¹Planetary Aeronomy, Belgian Institute for Space Aeronomy, 3 av. Circulaire, B-1180 Brussels, Belgium.

²Space Research Institute (IKI), 84/32 Profsoyuznaya Strasse, 117997, Moscow, Russia

³LATMOS, 11 Bd d'Alembert, 78280 Guyancourt, France ;

⁴Institut Pierre Simon Laplace, Université de Versailles-Saint-Quentin 78280 Guyancourt, France.

* Corresponding author: arnaud.mahieux@aeronomie.be

Keywords: planetary atmosphere, Venus, composition, retrieval, Echelle spectrometer, AOTF

Abstract

The SOIR instrument, flying onboard Venus Express, operates in the infrared spectral domain and uses the solar occultation technique to determine the vertical profiles of several key constituents of the Venus atmosphere. The retrieval algorithm is based on the Optimal Estimation method, and solves the problem simultaneously on all spectra belonging to one occultation sequence. Vertical profiles of H₂O, CO, HCl, and HF, as well as some of their isotopologues are routinely obtained for altitudes ranging typically from 70 to 120 km, depending on the species, and the spectral region recorded. In the case of CO₂, a vertical profile from 70 up to 150 km can be obtained by combining different spectral intervals. Rotational temperature is also retrieved directly from the CO₂ signature in the spectra. The present paper describes the method used to derive the above mentioned atmospheric quantities and temperature profiles. The method is applied on some retrieval cases illustrating the capabilities of the technique. More examples of results will be presented and discussed in a following companion paper which will focus on the CO₂ vertical profiles of the whole data set.

30 1. Introduction

31 Venus is known to be a very warm planet with a dense atmosphere. Its mesosphere extending from the cloud deck up to
32 ~ 100 km is composed mainly of carbon dioxide (CO_2 , 96.5%) and Nitrogen (N_2 , 3.5%). This region is dynamically and
33 photochemically very active, but has been up to now poorly observed. Previous measurements indeed focussed
34 essentially on the regions below the clouds down to the surface. The mesosphere acts as a transition region between the
35 lower atmosphere, and its cloud deck and super-rotational zonal winds, and the thermosphere, dominated by the subsolar
36 to antisolar circulation. The altitude of 100 km is a natural boundary in the atmosphere of Venus. The information
37 above 100 km altitude about temperature, pressure, the densities of carbon dioxide and other minor atmospheric
38 constituents, their sources and sinks, as well as the reactions in which they are involved, is incomplete, as only scarce
39 measurements have been performed [Clancy *et al.*, 2003; Sandor and Clancy, 2005; Clancy *et al.*, 2008]. Chemically
40 active species, such as sulphur-bearing gases (COS , SO_2) and halides (HCl , HF) have already been reported [de Bergh *et*
41 *al.*, 2006] but below 70 km altitude.

42 The SOIR (Solar Occultation in the InfraRed) spectrometer is an extension of the French instrument SPICAV, the
43 combination being called SPICAV/SOIR [Bertaux *et al.*, 2007; Svedhem *et al.*, 2007]. SPICAV/SOIR is one of the seven
44 instruments on board Venus Express (VEX), a planetary mission of the European Space Agency (ESA) that was
45 launched in November 2005 and inserted into a polar orbit around Venus in April 2006 [Titov *and al.*, 2006]. VEX is
46 orbiting around Venus on a polar orbit, which allows the instrument to sound almost all latitudes. The region comprised
47 between 40° and 60° North is however more difficult to sound due to the orbit shape.

48 SOIR is the first high-resolution near-infrared spectrometer on-board a spacecraft investigating the Venusian
49 mesosphere where it detected H_2O and HDO [Fedorova *et al.*, 2008], SO_2 [Belyaev *et al.*, 2008], HCl , HF , CO and CO_2
50 [Vandaele *et al.*, 2008]. [Belyaev *et al.*, 2008; Fedorova *et al.*, 2008; Vandaele *et al.*, 2008] The newness of such a
51 spectrometer and the high accuracy obtained allow us to measure Venus' atmosphere minor constituents as well as CO_2
52 absorption lines with a never-so-far obtained resolution from orbit. The solar occultation technique is used for the first
53 time at Venus. This technique has the advantage of being a self calibrated method, as will explained below in the text.
54 The retrieval method developed in this study will be discussed in details in terms of sensitivity and error sources. The
55 algorithm will be used to derive the atmospheric parameters from the spectra measured in two different regions during
56 an occultation: CO_2 , CO and temperature vertical profiles will be derived. We will also show that information on the
57 temperature can be retrieved directly from the spectra.

58 Comprehensive results considering CO_2 will be given in a companion paper [Mahieux *et al.*, 2010] in which the focus
59 will be made on temporal as well as latitudinal distribution of the CO_2 density and temperature.

60

61 2. The SOIR instrument

62 SOIR is an innovative, compact, high-resolution spectrometer for remote infrared measurements of gaseous species of
63 the Venus' atmosphere, which has been already extensively described [*Nevejans et al.*, 2006; *Mahieux et al.*, 2008;
64 *Mahieux et al.*, 2009]. A short description of its working principles will be given here. The system consists of an echelle
65 grating spectrometer working in the infrared (IR) combined with an acousto optic tunable filter (AOTF) for the selection
66 of diffraction grating orders. Such an instrument combines the advantages of a high spectral resolution, fast and flexible
67 access to any part of its spectral domain, compactness, no moving parts and low mass. The SOIR instrument is designed
68 to measure at high resolution ($\sim 0.15 \text{ cm}^{-1}$) the atmospheric transmission in the IR, between 2.2 and 4.3 μm (2200 –
69 4400 cm^{-1}).

70 The AOTF is driven by high radio frequencies (RF) that may be tuned for selecting the bandpass wavenumber range.
71 The AOTF is a fast-response solid state TeO_2 optical filter, whose transfer function has been extensively investigated in
72 [*Mahieux et al.*, 2009] and may be approximated by the sum of sinc squared functions, where $\text{sinc}(x)$ is defined as
73 $\sin(\pi x)/\pi x$, x being the independent variable, here the RF. The main lobe of the sinc square-like function has a full width
74 at half maximum (FWHM) of about 24 cm^{-1} . The shape of the AOTF transfer function varies significantly along the
75 wavenumber range [*Mahieux et al.*, 2009].

76 The echelle grating of SOIR divides the spectral range into 94 useful diffraction orders, ranging from 101 to 194. The
77 bandwidth varies from 19.3 cm^{-1} in diffraction order 101 to 37.1 cm^{-1} in order 194. The free spectral range (FSR) of
78 SOIR equals 22.38 cm^{-1} . In diffraction orders 101 to 122, the FSR is greater than the bandwidth, and hence, the detector
79 will lose part of the spectrum. The opposite occurs in diffraction orders 123 to 194, where only a part of the detector will
80 be covered by the diffracted order. Order overlapping occurs in these orders. The AOTF FWHM is greater than the FSR,
81 which will induce an additional contribution of the adjacent orders to the scanned order. The resolution of SOIR varies
82 from order to order, with a value of about 0.11 cm^{-1} in diffraction order 101 to 0.21 cm^{-1} in order 194.

83 The slit of SOIR is rectangular, with a viewing angle of 2° in the spectral direction, and 30° in the spatial direction. The
84 apparent size of the Sun at Venus is $44'$, which ensures that the slit will remain within the solar disc. The detector counts
85 320 pixels in the spectral direction and 256 pixels in the spatial direction called pixel rows further in the text. However,
86 the light coming from the aperture only covers 32 pixel rows in the spatial direction. From on-board measurements, it
87 has been observed that on these 32 pixel rows, the side rows have a very bad signal to noise ratio. For that reason only
88 the 24 central pixel rows are read. This has been applied to measurements which occurred after orbit 332 (March 19th,
89 2007). The pixel field of view varies between 0.03 and 0.06 cm^{-1} as a function of the pixel position and the diffraction
90 order.

91 Due to telemetry constraints, SOIR can only send 8 measurement packets per second. The AOTF and the electronics of
92 SOIR limit the number of orders to be measured to 4 orders per second. With all these constraints, six different cases
93 have been defined to sound Venus' atmosphere. The pixel rows are summed up and groups of pixel rows have been
94 defined. They are summarized in [Table 1Table 1](#).

95

96 [Table 1Table 1](#)

97

98 As an example, and throughout the following text, we will consider the 2x12 pixel rows case. As 4 diffraction orders can
99 be measured successively during one second, each order is scanned during 250 ms, and the same order is scanned once
100 in every second. Two groups of lines are defined, each group results of the sum of 12 pixel rows on the detector. This
101 operation improves also the signal to noise ratio. Typical values for the signal to noise ratio range between 500 and
102 3000.

103 As the SOIR instrument is able to measure at best 4 diffraction orders almost simultaneously during one solar
104 occultation, 4 different wavenumber ranges and therefore various species can be probed almost simultaneously.

105 **3. The solar occultation technique**

106 The solar occultation technique used by SOIR allows the derivation of unique information about the vertical structure
107 and composition of the Venus mesosphere [*Vandaele et al.*, 2008]. SOIR is looking towards the Sun and records spectra
108 on a one second cycle basis. Solar occultations occur when the line of sight of the instrument crosses the atmosphere of
109 Venus. The projection of the centre of the slit on the limbs during each single measurement defines the tangent altitude.
110 Because the spacecraft is moving along its orbit, the instrument sounds the atmosphere of the planet at different tangent
111 altitudes, see [Figure 1Figure 1](#). Two different configurations can be observed: the ingress case, when the tangent altitude
112 decreases with time, and the egress case, when the tangent altitude increases with time. For the sake of simplicity, only
113 the ingress case will be described here. The egress case may be considered as ingress with the time scale reversed.

114 The instrument is turned on and, after a pre-cooling phase to ensure that the detector temperature has reached its
115 operating value of about 70 K, it starts recording solar spectra before the line of sight crosses the atmosphere. It is
116 assumed that the atmosphere of Venus extends up to 220 km in altitude [*Hedin et al.*, 1983]. This procedure starts early
117 enough, corresponding to tangent altitudes well above 220 km, to obtain an amount of at least 40 spectra taken outside
118 the atmosphere. They define the reference Sun spectrum. A regression is calculated on each pixel of these recorded
119 spectra to remove the small intensity drift observed. This operation reduces the systematic errors, and results in a higher

120 signal to noise ratio. For tangent altitudes lower than 220 km, the atmospheric transmittances are calculated by dividing
121 the spectrum recorded at the current time by the reference Sun spectrum.

122 The wavenumber calibration, i.e. converting pixel number of the detector to wavenumber using the position of known
123 solar lines, includes a correction for the Doppler effect, as the speed of the satellite projected on the line of sight may
124 vary during an occultation, but also from one orbit to the other. Indeed, the speed of the satellite often gets close to +/-
125 10 km/s, depending of the relative position of the Sun and VEX, which may result in slight displacements of the solar
126 lines, used for the calibration.

127 When SOIR points towards the Sun, the position of the slit with respect to Venus is set in order to have its spatial
128 direction parallel to the limb of Venus, when the tangent altitude reaches 60 km. The slit should remain as parallel as
129 possible to the limb in order to have the smallest vertical resolution for each separate measurement. Since the VEX
130 satellite is set into an inertial mode while performing a solar occultation, the slit rotates slightly, and does not remain
131 parallel to the limb during the whole occultation. This tilting angle remains small, reaching maximum values in some
132 occultations of about 10°, which slightly decreases the vertical resolution.

133 The orbit of Venus Express is very eccentric with its apocenter, located above the North Polar Region, at an altitude of
134 180 to 250 km above the ground. The pericenter, above the South Polar Region, reaches 65,000 km. For this reason, the
135 vertical resolution of the measurement, which depends on the distance of the satellite to the limb, will also be dependent
136 on the latitude of the measurement : high Northern latitude (60° to 90°) measurements have a very good vertical
137 resolution, the layer thicknesses are small (from 200 m to 700 m); measurements at lower latitudes (-30° to 60°) have an
138 average vertical resolution ranging from 700 m to 2 km; Southern latitudes (-90° to -30°) have a very poor vertical
139 resolution, with layer thicknesses greater than 2 km, up to 5 km.

140 Method description

141 The analysis code is based on the ASIMUT program [*Vandaele et al.*, 2008] and has been adapted in Matlab in order to
142 improve the retrieval procedure, i.e. by allowing the determination of the temperature, and allowing more flexibility. The
143 algorithm uses the onion peeling approach. This simplifies the problem, as for a given layer the physical properties only
144 depend on the layers located below itself [*Russel and Drayson*, 1972]. The method will be described for the retrieval of
145 the vertical density profile of a given molecule. In the cases of carbon dioxide and carbon monoxide retrievals, we will
146 show how information can be obtained about molecular rotational temperature. The attitude of VEX is calculated using
147 the Spice for Matlab routines developed by NAIF (NASA Ancillary Information Facility) [*NAIF*, 2009], and used by
148 ESA for the Venus Express mission.

149 3.1 Tangent altitude and ray tracing

150 The tangent altitude of each measured transmittance of one occultation series defines the atmospheric layers used in the
151 onion peeling method, see [Figure 1](#)~~Figure-1~~. The tangent altitude is computed from the geometry of the pointing of the
152 instrument relative to the Sun and the planet Venus as illustrated in [Figure 2](#)~~Figure-2~~. The centre of the projected slit is
153 taken as a reference, see [Figure 3](#)~~Figure-3~~. In this frame, the relation used to calculate the tangent altitude (H_{tg}), when no
154 refraction is taken into account, is

$$H_{tg} = \cos(\pi - \alpha) \cdot R_{VV} \quad (1)$$

155 where R_{VV} is the distance from the satellite to the centre of Venus and α is the pointing angle to the centre of the
156 projected slit, taking into account the 10' depointing to the centre of Sun, see [Figure 2](#)~~Figure-2~~. The ray tracing
157 calculation allows the determination of the tangent height and of the absorption path in each of the layers, taking into
158 account the refraction of the light beam into the atmosphere. The refraction model is based on the measurements
159 performed during the Magellan mission. The refraction is calculated as described in [Vandaele *et al.*, 2008]. The
160 determination of the radiation path through the atmosphere, i.e. the path followed by the radiation reaching the
161 instrument, requires that the planet's curvature and refraction be taken into account. The model is based on the ray-
162 tracing program FSCATM [Gallery *et al.*, 1983]. Some modifications were included in the implementation, essentially
163 dealing with the determination of the index of refraction of the air of the planet. Integrated total density, integrated
164 partial density of the molecules fitted, mean local temperature, integrated local pressure and path length are computed
165 for each layer. They are also corrected by accounting for the height of the projected slit in the atmosphere at each
166 measurement.

167

168 [Figure 1](#)~~Figure-1~~

169 [Figure 2](#)~~Figure-2~~

170

171 As already stated, due to telemetry limitations, the detector is divided into several groups of lines, also called bins. The
172 pointing directions are calculated for each of these bins separately. In our example, case 2x12, there are 2 bins, each
173 made up of 12 detector rows. The size of the whole slit being 30', along the spatial direction, by 2', along the spectral
174 direction, the centre of bin 1 is slightly depointed depending on the tilting angle γ , see [Figure 3](#)~~Figure-3~~.

175

176 [Figure 3](#)~~Figure-3~~

178 3.2 Absorption cross section and transmittance calculation

179 Molecular absorption cross sections (ACS) in each layer are calculated by a line by line procedure, extensively described
 180 in [Vandaele *et al.*, 2008], using spectroscopic parameters from Hitran 2008 [Rothman *et al.*, 2009] adapted for the
 181 Venusian CO₂-rich atmosphere. The absorption cross sections depend on the partial and total pressures, as well as on the
 182 temperature in each layer. The transmittance due to molecule i in the layer j is calculated using:

$$T_{i,j} = \exp\left[-n_{i,j} \cdot s_j \cdot ACS(n_{i,j}, t_j, p_j)\right] \quad (2)$$

183 where $n_{i,j}$ is the density of the molecule i in the layer j , s_j is the path length within the layer j , and t_j and p_j are the
 184 temperature and the pressure in the layer j , obtained as explained in Section 3.1 from the ray tracing algorithm.

185 The transmittance $T_{L,Molecular}$ due to the molecular species present along the whole path corresponding to the tangent
 186 height L is finally obtained by multiplying the absorbance of all molecules in all the above layers, the most outside layer
 187 being layer 1:

$$T_{L,Molecular} = \prod_{j=1}^L \prod_{i=1}^{n_{molecules}} T_{i,j} \quad (3)$$

188 Aerosols, which are present in the Venus atmosphere in large quantities [Esposito, 1983; Lane and Opstbaum, 1983],
 189 also have a characteristic signature. In the infrared region probed by SOIR their signature is large, but broad and without
 190 fine structures [Wilquet *et al.*, 2009]. Their influence on the observed spectra is to decrease the mean transmittance level.
 191 This effect is more pronounced as the line of sight goes deeper into the atmosphere.

192 The impact of aerosols is considered by representing their contribution to the transmission by a second degree
 193 polynomial on the wavenumber. For layer L , the aerosol contribution can be written as:

$$T_{L,Aerosols} = a_L + (\omega_n - \omega_{n_0}) \cdot b_L + (\omega_n - \omega_{n_0})^2 \cdot c_L \quad (4)$$

194 where a_L , b_L and c_L are the polynomial coefficients, ω_n is the wavenumber, ω_{n_0} is the central wavenumber of the
 195 scanned order.

196 The aerosol extinction can be calculated from the parameters a_L [Bingen *et al.*, 2003]. The results have already been
 197 discussed in [Wilquet *et al.*, 2009], and will be deeper analysed in a future publication [Wilquet *et al.*, 2010].

198 Finally, the synthetic spectrum I_L , which will be compared to the one recorded by the instrument, is the solar spectrum
 199 attenuated by the effect of the atmospheric molecular species and aerosols, convolved by the instrumental function:

$$I_L = conv \left(\underbrace{I_{Sun} \cdot T_{L,Aerosols} \cdot T_{L,Molecular}}_{\text{synthetic spectrum}}, \underbrace{Gauss(Resol_{SOIR})}_{\text{instrument function}} \right) \quad (5)$$

200 with I_{Sun} the Sun absorption cross section and $Gauss(Resol_{SOIR})$ the instrument function with the spectral resolution
 201 function of SOIR [Mahieux et al., 2008].

202 Even if the resolution of SOIR is good enough to resolve most of the atmospheric absorption lines, it remains a few
 203 factors larger than the width of the pressure broadened atmospheric absorption lines. Therefore the pressure can not be
 204 deduced from the measured spectrum. This is mathematically illustrated by the convolution product in Equation (5)
 205); the synthetic spectrum has a FWHM of about 0.001 cm^{-1} to 0.01 cm^{-1} , while the resolution of SOIR is about 0.15 cm^{-1} .

206 3.3 Order addition

207 The bandwidth of SOIR's AOTF, used for the diffraction order selection, is larger than the free spectral range of the
 208 echelle grating. To correctly simulate the spectra measured by the spectrometer, the contribution of the adjacent orders
 209 also has to be taken into account. Usually, the two first adjacent orders and the central order are considered to form most
 210 of the observed transmittance. In some cases, however, when very strong lines are present in adjacent orders located
 211 further away from the central order, it may be necessary to consider a larger number of adjacent orders. Usually, 3
 212 diffraction orders are taken into account. The contribution from the adjacent orders is calculated using:

$$T = \frac{\sum_{i=-n_{orders}}^{n_{orders}} AOTF_i \cdot I_L}{\sum_{i=-n_{orders}}^{n_{orders}} AOTF_i \cdot I_{Sun}} \quad (6)$$

213 where T is the transmittance, n_{orders} is the number of adjacent orders considered, $AOTF_i$ is the values of the AOTF
 214 transfer function in the order i and I_i is the convoluted absorbance of the molecules and aerosols absorbing in order i
 215 [Mahieux et al., 2009]. The whole procedure for constructing a synthetic spectrum is depicted in Figure 4

216 **Reference source not found.**

217

218 **Figure 4** **Reference source not found.**

219

220 **4. Retrieval algorithm**

221 The Optimal Estimation (OE) method developed by Rodgers [Rodgers, 1990; Rodgers, 2000] has been implemented to
 222 inverse the observed transmittances. All transmittances, corresponding to one occultation series considered after the
 223 selection procedure, are inverted in one go.

224 **4.1 Implementation of the OE algorithm**

225 The transmittance in a given layer L is given by:

$$T_L = \frac{\sum_{p=-n_{orders}}^{n_{orders}} AOTF_p \cdot conv\left\{I_{Sun} \cdot T_{L,Aerosols} \cdot \prod_{j=1}^L \prod_{i=1}^{n_{molecules}} \exp\left[-n_{ij} \cdot s_j \cdot ACS_{ij}\left(n_{ij}, t_j, \omega'_{n_j}\right)\right], Gauss(\sigma_{SOIR})\right\}}{\sum_{p=-n_{orders}}^{n_{orders}} AOTF_p conv\{I_{Sun}, Gauss(\sigma_{SOIR})\}} \quad (7)$$

$$T_{L,Aerosols} = a_L + (\omega_n - \omega_{n_0}) \cdot b_L + (\omega_n - \omega_{n_0})^2 \cdot c_L$$

$$\omega'_{n_j} = \omega_n + d_j$$

226 where T_L is the transmittance at the layer L , $AOTF_p$ is the modified AOTF transfer function, adapted on the n_{AOTF} points
 227 and translated of a value d_{AOTF} , d_i is the wavenumber shift of layer j and σ_{SOIR} is the resolution of the instrument. In this
 228 Equation, n_{ij} , t_j , a_L , b_L , c_L , $AOTF_p$, d_{AOTF} and d_j are unknown variables.

229 In order to fit T_L to the measured spectra, the problem is written in the form

$$y = F(x, b) + \varepsilon \quad (8)$$

230 where y is the measurement vector (the measured transmittances), x is the state vector (all unknown variables to be
 231 retrieved, f.e. the vertical density profiles), b represents the additional parameters used by the forward model, whose
 232 function is F . The forward function F describes the complete physics of the measurement, including the description of
 233 the instrument. F is the set of L functions T_L described in Equation (7). ε represents the noise on the
 234 measurement.

235

236 Let us consider the retrieval of the vertical profiles of $n_{molecules}$ from a series of $n_{spectra}$ transmittances acquired during one
 237 occultation. The $n_{spectra}$ spectra have defined a structured atmosphere composed of $m_{layer} = n_{spectra}$ layers (see [Figure](#)
 238 [1Figure 1](#)), whose boundaries correspond to the tangent heights of each measurement. The state vector contains all the
 239 variables fitted during the retrieval procedure. These variables are the a , b and c parameters of the aerosol contribution
 240 ($3 \times m_{layer}$ variables), and the logarithm of the molecular densities of the targeted species in all the defined layers
 241 ($n_{molecules} \times m_{layer}$ variables). The temperature in each layer may also be fitted (m_{layer} variables). Even if the line intensities
 242 of all molecules are temperature dependent, the temperature is only fitted for molecules having regularly spaced

243 absorption lines or absorption lines close to each others, such as CO or CO₂. Moreover a wavenumber shift can be
 244 introduced and fitted for each spectrum (m_{layer} variables) to improve the matching of the absorption lines positions from
 245 the spectroscopic database and the observed position. The AOTF transfer function may be fitted too: First, a slight
 246 variation is allowed on several points, usually around 40, to improve the quality of the fit (n_{AOTF} variables); Second, the
 247 AOTF transfer function may also be translated along the wavenumber axis, to correct for possible deviations of the
 248 wavenumber – AOTF frequency relation [Mahieux *et al.*, 2008] (1 variable). It leads to a total number of variables of
 249 $n_{var} = (5 + n_{molecules}) \cdot m_{layer} + n_{AOTF} + 1$.

250 The Rodgers formalism solves the problem written in Equation (8)(8) by starting from an a-priori value of the
 251 variable x iterating on the following Equation:

$$x_{k+1} = x_k + (S_a^{-1} + K_k^T S_\varepsilon^{-1} K_k)^{-1} [K_k^T S_\varepsilon^{-1} (y - F(x_k)) - S_a^{-1} (x_k - x_a)] \quad (9)$$

252 where x_k are the state vector values at iteration k , S_a is the covariance matrix of the fitted parameters, S_ε is the
 253 measurement error matrix, K_k is the Jacobian of the problem at iteration k , y contains the measured spectra, F is the
 254 forward model of Equation (8)(8) and x_a is the a-priori state vector.

255 The covariance matrix S_a contains the allowed variability of each variable:

$$S_a = \varepsilon \{ (x - x_a)(x - x_a)^T \} \quad (10)$$

256 where x_a is the a-priori state vector and x is the solution of the problem. Non diagonal terms are added for the covariance
 257 of the densities, temperature, wavenumber shift and AOTF transfer function variations. A Gaussian dependence is used
 258 to account for correlations between the different points where the AOTF transfer function is fitted and to ensure a final
 259 smooth AOTF transfer function. They are defined as:

$$S_a^\omega(i, j) = \sqrt{S_a^\omega(i, i) \cdot S_a^\omega(j, j)} \cdot \exp \left[- \left(\frac{\omega_{n_i} - \omega_{n_j}}{l_\omega} \right)^2 \right] \quad (11)$$

260 where S_a^ω is the submatrix of S_a corresponding to the AOTF transfer function fit, ω_{n_i} is the wavenumber position of
 261 point i , l_c is the correlation length [Vandaele *et al.*, 2006]. The correlation length has been chosen to be a fifth of the
 262 diffraction order width for the AOTF transfer function. In the case of the densities, temperature and wavenumber shift,
 263 the coefficients are:

$$S_a^{n,t,d}(i, j) = \sqrt{S_a^{n,t,d}(i, i) \cdot S_a^{n,t,d}(j, j)} \cdot \exp \left[- \left(\frac{z_i - z_j}{l_z} \right)^2 \right] \quad (12)$$

264 where $S_a^{n,t,d}$ is the submatrix of S_a corresponding to the density, temperature or wavenumber shift variables, z_i is the
 265 altitude of point i and l_z is the correlation length, defined as the height of the projected slit at the tangent point. In the
 266 case of the aerosols contribution only diagonal terms are considered. S_a is a square matrix of size n_{var} .

267 The measurement error matrix S_ϵ contains the estimated errors calculated from the signal to noise ratio. S_ϵ is not square
 268 and has a size of $n_{\omega_n} \cdot m_{\text{layer}}$, where n_{ω_n} is the number of wavenumber points in each interval used for the fit.

269 The Jacobian matrix K contains the first derivatives of the forward model with relation to all the state vector variables.
 270 The derivatives

$$\frac{\partial T}{\partial a_L}, \frac{\partial T}{\partial b_L}, \frac{\partial T}{\partial c_L}, \frac{\partial T}{\partial n_{ij}}, \frac{\partial T}{\partial t_j}, \frac{\partial T}{\partial d_j}, \frac{\partial T}{\partial n_{AOTF}}, \frac{\partial T}{\partial d_{AOTF}} \quad (13)$$

271 are easily computed. They are all derived analytically, except for the displacement derivatives $\frac{\partial T}{\partial d_j}$, which are
 272 calculated numerically.

273 The sub matrices of K , $\frac{\partial T}{\partial n_{ij}}$, $\frac{\partial T}{\partial t_j}$ and $\frac{\partial T}{\partial d_j}$, are inferior triangular matrices because of the onion peeling procedure.

274 $\frac{\partial T}{\partial d_{AOTF}}$ is a vector, as $\frac{\partial T}{\partial a_L}$, $\frac{\partial T}{\partial b_L}$, $\frac{\partial T}{\partial c_L}$ which have non-zero values only for a given layer. $\frac{\partial T}{\partial n_{AOTF}}$ is a full matrix. K

275 has a size of $n_{\text{var}} \times (n_{\omega_n} \cdot m_{\text{layer}})$. The vectors x_k , x_a , $F(x_i)$ and y contain respectively the state vector variables at step k ,

276 the a-priori values of the variables x_k , the calculated transmittance at step k and the n_{spectra} observed spectra. The vectors

277 x_k , x_a have a length of n_{var} , while the vectors $F(x_i)$ and y have a length of $(n_{\omega_n} \cdot m_{\text{layer}})$.

278 The convergence of the algorithm is achieved when the following criterions are both satisfied

$$\begin{aligned} (x^t - x^{t-1}) \cdot (S_a^{-1} + K' \cdot S_\epsilon^{-1} \cdot K)^{-1} \cdot (x^t - x^{t-1}) &< 0.001 \cdot n_{\text{var}} \\ (F^t - F^{t-1}) \cdot (S_\epsilon \cdot K \cdot S_a \cdot K' \cdot S_\epsilon) \cdot (F^t - F^{t-1}) &< 0.001 \cdot n_{\omega_n} \cdot m_{\text{layer}} \end{aligned} \quad (14)$$

279 where x^t and F^t are respectively the state vector and the function described in Equation 10.

280 The error calculation is done using the relations:

$$\begin{aligned} \hat{x} - x &= (A - I_n) \cdot (x - x_a) + G \cdot \epsilon \\ G &= [(S_a^{-1} + K^T \cdot S_\epsilon^{-1} \cdot K) \cdot K^T \cdot S_\epsilon^{-1}]^{-1} \\ A &= G \cdot K \end{aligned} \quad (15)$$

281 where $\hat{x} - x$ is the error vector, x is the solution at convergence and \hat{x} is the exact solution, I_n is a unity matrix having

282 the same size as A and ϵ is the error vector used to build S_ϵ .

283 The covariance of the error vector is built by considering two sources, namely the a-priori covariance S_s and the retrieval
 284 noise covariance S_m :

$$\begin{aligned} S_s &= (S_a^{-1} + K^T \cdot S_\epsilon^{-1} \cdot K)^{-1} \cdot S_a^{-1} \cdot (S_a^{-1} + K^T \cdot S_\epsilon^{-1} \cdot K)^{-1} \\ S_m &= (S_a^{-1} + K^T \cdot S_\epsilon^{-1} \cdot K)^{-1} \cdot K^T \cdot S_\epsilon^{-1} \cdot K \cdot (S_a^{-1} + K^T \cdot S_\epsilon^{-1} \cdot K)^{-1} \end{aligned} \quad (16)$$

285 **4.2 Fitting procedure**

286 For a given occultation and a given diffraction order, the spectroscopic parameters of the different species to retrieve
 287 must be supplied, as well as the wavenumber range on which they will be fitted. More than one isotopologue for each
 288 species may be fitted simultaneously. The altitude range is automatically determined, but may also be imposed by the
 289 user.

290 The algorithm returns the fitted values of all the parameters defined earlier. The user has the choice to use the a-priori
 291 atmospheric parameters derived from the atmosphere model, or to use the ones derived from another fitting procedure,
 292 for example a quasi simultaneous CO₂ inversion.

293 **4.3 Predetermination of the useful altitude range**

294 We have developed an automatic procedure to determine the useful altitude range of the retrieval of one given
 295 occultation. Usually, atmospheric spectra are recorded at tangent altitudes starting around 220 km and down to 60 km.
 296 However, the spectra corresponding to the higher altitudes usually do not contain any absorption features, but provide a
 297 good indication of the noise level of the measurements, and spectra corresponding to the lowest altitudes are often
 298 saturated due to too high atmospheric absorption as detailed in the following.
 299 The first spectrum considered for the retrieval corresponds to the emergence of the monitored absorption structures.
 300 Only the wavenumber range on which the retrieval is performed is considered. The maximum (I_{\max}), minimum (I_{\min})
 301 and mean (I_{mean}) values of the transmittance are computed on this window for each atmospheric spectrum. The depth of
 302 the strongest observed line (I_{diff}) is computed by subtracting the minimum value from the maximum value
 303 ($I_{\text{diff}} = I_{\max} - I_{\min}$). At high altitudes, usually above 180 km, just before the emergence of the absorption features, only
 304 noise is measured, and I_{diff} provides a good estimate value for it. A signal to noise value ($\overline{SNR}_{180-220}$) representative of
 305 these high altitudes is calculated by considering the average values of the signal and of the noise between 220 km and
 306 180 km, $\overline{I_{\text{mean}}}$ and $\overline{I_{\text{diff}}}$,

$$SNR_{180-220} = \frac{\overline{I_{\text{mean}}}}{\overline{I_{\text{diff}}}} \quad (17)$$

307 The first spectrum to consider for the retrieval procedure corresponds to the altitude when the absorption structures are
 308 seen above the noise. From trials, a factor of 0.002 has been introduced, thus the first spectrum is defined for

$$\frac{I_{mean}}{I_{diff}} < 0.002 \cdot SNR_{180-220} \quad (18)$$

309 From this altitude and below, spectral structures are seen in the spectra.

310 The lower bound of the altitude range is defined when saturation occurs: the atmospheric absorption lines have
 311 transmittances reaching zero values at their centre, before convolution by the instrument resolution function. From this
 312 altitude, the information contained in the spectra becomes useless, and reliable retrievals can not be made.

313 The criteria used for the selection of first and last spectra are clearly demonstrated when plotting the quantity $\frac{I_{mean}}{I_{diff}}$ as a

314 function of the altitude, as illustrated in [Figure 5](#). The slope radically changes at two well defined altitudes.

315 Values of $\frac{I_{mean}}{I_{diff}}$ are almost constant above the altitude of point 2 on Panel C corresponding to the appearance of the

316 absorption features as illustrated by the Panels A and B, corresponding respectively to one spectrum without absorption

317 structures and one with them. The altitude of the last spectrum to be included in the retrieval, point 3 on Panel C, is

318 obtained at the second change in slope. Below this altitude, most of the absorption lines are saturated – at infinite

319 resolution – and the surface under the structures seen in the convolved spectrum recorded by the instrument are no

320 longer proportional to the density of the absorbing species.

321

322 [Figure 5](#)

323

324 Saturation may be observed if the transmittance of a spectral line reaches values close to zero. In that case, all the

325 information contained in the observed spectral line is lost, as the shape of the line does not vary with increasing

326 densities. It is not directly observed on the spectra measured by SOIR, as the resolution of the instrument is much larger

327 than the width of the observed spectral lines. Detection procedures of such events have been developed, to avoid

328 meaningless density profiles. All absorption lines having a transmittance (at infinite resolution) lower than 0.15 are

329 considered as saturated [*Vander Auwera*, Private communication]. The transmittance before convolution and order

330 addition $\tilde{T}_L(\omega_n)$ is defined as

$$\tilde{T}_L(\omega_n) = \prod_{j=1}^L \prod_{i=1}^{n_{molecules}} \exp \left[-n_{ij} \cdot s_j \cdot ACS_{ij} \left(n_{ij}, t_j, \omega_{n_j} \right) \right] \quad (19)$$

331 If saturation occurs, two actions are taken: (i) all the points ω_n^* for which we have $\tilde{T}_L(\omega_n^*) < 0.15$ are removed from
332 the fitted wavenumber range; (ii) the spectrum of layer j^* at iteration k of the Rodgers algorithm is said to be saturated
333 if more than 40 percent of the absorption lines coming from the central order are saturated, or 40 percent of the detector
334 is covered by saturated lines. In that case, the altitude range is modified to suit the saturation criterion: all the layers j
335 located under and including the current layer j^* are excluded from the retrieval, i.e. for $j^* \leq j \leq m_{layer}$. To that end, the
336 corresponding lines and columns are removed from the S_a , K , S_e , Y , F , x_k and x_a matrices or vectors. That condition is
337 evaluated at each step of the OE algorithm.

338 However, the aerosol background can be retrieved for the layers in which saturation occurs, if the saturated lines are
339 removed from the wavenumber fitted range. The variables a , b and c of the aerosol background are thus retrieved on the
340 entire occultation, while the density, temperature and displacement are only retrieved in the non saturated altitude range.

341 **4.4 Model of the atmosphere**

342 In this work, we have used temperature and pressure vertical profiles from the VIRA model for altitudes up to 100 km
343 [Seiff *et al.*, 1985]. For higher altitudes (from 140 km and upwards), data were taken from the model of [Hedin *et al.*,
344 1983] as suggested in [Mueller-Wodarg and Tingle, 2008]. The transition between the two data sets was performed by
345 splines interpolating the temperature and reconstructing the pressure through the hydrostatic law.

346 **4.5 Temperature dependence**

347 SOIR spectra are sensitive to the atmospheric temperature through its influence on the strength of the absorption features
348 of, for example, CO or CO₂. Temperature will influence the overall shape of one specific vibrational band, as shown in
349 [Figure 6](#). Each peak belongs to a given rotational transition J . If temperature increases the position of the band
350 absorption maximum will move from low J lines to higher J lines, as the distribution of line intensities for different
351 rotational transition changes. From the overall shape, temperature can then be derived even if some of the information
352 contained in this shape disappears because of the curvature of the AOTF transfer function, as illustrated in [Figure](#)
353 [6](#).

354 This approach leads to the determination of the rotational temperature of the gas in one vibrational band. Local
355 thermodynamical equilibrium (LTE) needs to be satisfied in order to assimilate the rotational temperature to the kinetic
356 temperature, which may not be necessarily the fact [Gilli *et al.*, 2009]. However, the non-LTE effects only weakly affect
357 ground state rotational transition bands [Lopez-Valverde, Private communication].

358 The shape of the AOTF function will thus influence the temperature retrieval, as a good knowledge of the function is
 359 needed in order to correctly build the synthetic spectrum. However, the correction of the AOTF function using the n_{AOTF}
 360 points as described in Section 4.1 will only locally modify the transfer function, and thus not the overall shape.

361

362 [Figure 6](#)

363

364 4.6 Wavenumber scale definition

365 Using the theoretical relations of the echelle grating, a linear relationship between the wavenumber, the order and the
 366 pixel number can be defined [Schroeder and Hilliard, 1980; Nevejans et al., 2006; Mahieux et al., 2008]:

$$\begin{cases} d(\sin \theta_i + \sin \theta_m) = m \cdot \lambda \\ \lambda = 10^{-2} / \omega_n \\ pixel = f(\theta_m) \end{cases} \Rightarrow pixel = f \left[\arcsin \left(\frac{m \cdot 10^{-2}}{d \cdot \omega_n} - \sin \theta_i \right) \right] \quad (20)$$

367 where θ_i is the incident angle on the grating, θ_m is the refracted angle on the grating, m is the diffraction order, λ is
 368 the wavelength, d is the groove spacing of the echelle grating and f is a linear function linking the diffracted angle and
 369 the pixel number.

370 The calibration has been performed by comparing the positions of selected solar lines observed by SOIR outside the
 371 Venus atmosphere with a reference atlas of solar lines [Altieri et al., 2009], taking into account a correction applied to
 372 the observed solar lines for the Doppler effect induced by the motion of Venus Express relative to the Sun. Indeed, the
 373 satellite is orbiting around Venus at a speed which is varying significantly. The speed at apogee may reach absolute
 374 values of 10 km/s relative to Venus. The speed vector has to be projected onto the line of sight of the SOIR instrument.
 375 The sign of the speed may be positive or negative, depending of the satellite movement direction relative to the Sun.

$$\omega_n' = \omega_n \cdot \left(1 + \frac{v_{VEX}}{c} \right) \quad (21)$$

376 where ω_n is the wavenumber position of the line – taken from the solar atlas, v_{VEX} is the speed of the Venus Express
 377 satellite relative to Venus projected onto the line of sight of the instrument, c is the speed of light and ω_n' is the
 378 wavenumber corrected for the Doppler effect. The rotation of the planet itself is not taken into account, as its speed is
 379 very low: about 1.811 m/s at the equator. The speed of the planet Venus around the Sun projected onto the line of sight
 380 may be neglected during an occultation, as the eccentricity of the orbit of Venus is very small (~ 0.00677323).

381 After these corrections, it has been observed that small variations remain when considering the coincidence of the
382 observed and database absorption lines. The justification comes from small temperatures variations within the
383 instrument that may induce such variations to the above described calibration. The residual is fitted using the relation

$$\omega_n'' = \omega_n + (e + f \cdot (\omega_n - \omega_{n0})) \quad (22)$$

384 where e and f are the coefficients of a first order polynomial. These two variables are fitted on the whole occultation,
385 meaning they have the same value for all m_{layer} spectra. For this reason, they are independent of the wavenumber shifts
386 of each layer d_i .

387 **4.7 Measurement error and pointing error**

388 Two external independent sources of errors, coming from different sources are considered in the present work: the
389 measurement error and the satellite pointing error.

390 The first one, the measurement error calculation, has been described in [Mahieux *et al.*, 2008]. The signal to noise ratio
391 obtained is very good, reaching average values of around 500 up to 3000.

392 The second one, the satellite pointing error, is obtained directly from ESOC¹, the European Space Operation and Control
393 of the European Space Agency, which provides the pointing angle error, from which the altitude error is computed. The
394 largest error values at the limb are of the order of 500 m for orbits when the satellite is far away of the planet, and less
395 than 50 m while the satellite is close to the planet.

396 **5. Examples of applications**

397 In the following we will illustrate the method developed above with two different retrieval cases. The focus is placed on
398 the analysis of the method and its merits. Further scientific discussion on the results, considering a more complete data
399 set, will be pursued in the second part of this series.

400 **5.1 Carbon dioxide retrieval**

401 One order per occultation has been systematically dedicated to carbon dioxide measurements. The diffraction order 149
402 ($3329.8 - 3358.3 \text{ cm}^{-1}$) corresponds to a spectral interval in which the main isotopologue $^{16}\text{O}^{12}\text{C}^{16}\text{O}$ presents a relatively
403 strong absorption band. As mentioned in [Vandaele *et al.*, 2008], this band allows us to cover tangent altitudes from
404 about 75 km up to 120 km. But saturation of the lines generally restricts the minimum altitude to approximately 100 km.
405 To simulate this order, the adjacent orders +1 and -1 are taken into account, ranging from 3307.47 cm^{-1} to 3380.86 cm^{-1} .
406 The resolution of the instrument in this region is 0.16 cm^{-1} . The three most important bands in intensity, which are

¹ <ftp://ssols01.esac.esa.int/pub/data/GDP/VEX/ATTDEV/>

436 included in the simulation, are the 21102-00001, 22202-01101 and 30003-01101 transitions, having maximal intensities
437 of $9.1 \times 10^{-22} \text{ cm}^{-1}/(\text{molecule cm}^{-2})$, $4.4 \times 10^{-24} \text{ cm}^{-1}/(\text{molecule cm}^{-2})$ and $1.3 \times 10^{-24} \text{ cm}^{-1}/(\text{molecule cm}^{-2})$, respectively
438 comprising 306 lines in total. [Figure 8](#) shows the coverage of this order measurement.

439

440 [Figure 7](#)

441 [Figure 8](#)

442

443 A complete description of the retrieval of orbit 341 (28/03/2007) is given in the following. [Table 2](#) summarizes
444 the orbit information, while [Figure 7](#) depicts all the spectra measured in the four scanned diffraction orders. The
445 measurements were taken between 06:20:01 and 06:29:54 AM, during an egress case of the satellite. The latitude at the
446 tangent altitude of 65 km was 82.05° , and the longitude was 348.20° . The local solar time was 17.30. The speed of the
447 satellite projected on the line of sight was -8.76 km/s . The useful altitude range for the retrieval extended from 102.7 km
448 up to 120.0 km, resulting from the criteria developed before. The vertical profiles for the CO_2 density and the
449 temperature are given in [Figure 9](#). [Figure 10](#) illustrates the quality of the fit, which is performed on
450 only a portion of the recorded spectra (green curve). The layers below 102.7 km have been removed because some of the
451 lines were saturated, and were not fulfilling the criteria described in Section **Error! Reference source not found.** The
452 averaging kernels for the main fitted parameters are presented in [Figure 11](#). As expected, the averaging kernels
453 corresponding to the background parameters (a , b , and c , not shown for the latter) are only defined at the level to which
454 they correspond.

455 The averaging kernels or the CO_2 concentrations have maximum values increasing while going deeper in the
456 atmosphere, because there is more spectroscopic information present in the spectra: the path length is longer and the
457 density is higher for low altitude measurements. It may also be observed that the highest altitude kernels are also defined
458 at the surrounding altitudes, corresponding to the fact that they influence as well the layers located below them. The
459 averaging kernel for the wavenumber shift is much more intricate, as a shift in a layer will partially influence all the
460 other layers. No direct conclusion can be drawn in this case.

461 The error covariances matrices have been calculated for the baseline parameters a , b and c , the CO_2 density, the
462 temperature and the AOTF fitted values. The error covariances of a , b , c and wavenumber shift parameters are diagonal
463 matrices, as the parameter of a given layer does not depend on the other layers parameters. The influence of the other
464 layers on the density parameters is observed in its error covariance matrix by showing non-zero values outside the

Formatted:

465 diagonal: the upper layers have an influence on the lower layers, coming from the onion peeling method. It is not
466 observed for the error covariances of the temperature, as the temperature dependence is weak.

467

468 [Figure 9](#)~~Figure 9~~

Formatted:

469 [Figure 10](#)~~Figure 10~~

Formatted:

470 [Figure 11](#)~~Figure 11~~

Formatted:

471

472 The vertical profiles described here above cover an altitude range between 120 and 102.7 km. As explained before, the
473 retrieval can take place in a given order when the absorption features appear in the spectra, and is stopped when
474 saturation of the absorption lines occurs. Using other diffraction orders, other CO₂ bands with different line intensities
475 can be investigated, allowing a wider vertical coverage. This is illustrated in [Figure 12](#)~~Figure 12~~ and [Figure 13](#)~~Figure 13~~
476 where the densities of CO₂ and the rotational temperature obtained using different orders in quasi consecutive orbits are
477 presented.

Formatted:

478

479 Figure 12

480 Figure 13

481

482 5.2 Carbon monoxide retrieval

483 The main isotopologue ¹²C¹⁶O of carbon monoxide presents some absorption features in diffraction order 190 (4246.1 –
484 4282.4 cm⁻¹). Two transitions are considered: the (2-0) band, with 28 lines and a maximum intensity of
485 4.5x10⁻²¹ cm⁻¹/(molecule cm⁻²) and the (3-1) band with 21 lines and a maximum intensity of
486 3.2x10⁻²⁸ cm⁻¹/(molecule cm⁻²). To simulate this order, the adjacent orders +1 and -1 are taken into account, ranging from
487 4223.7 cm⁻¹ to 4305.0 cm⁻¹. The resolution of the instrument in this region is 0.23 cm⁻¹.

488 Order 190 was scanned during occultation 341, the same one used to illustrate the retrieval of CO₂.

489 The preliminary altitude range was defined from 119 km down to 65 km, but during the fit it has been reduced to 119 km
490 down to 99.7 km, because of the saturation occurring at the lower altitudes. Similar to what has been shown for the CO₂
491 results; [Figure 14](#)~~Figure 14~~, [Figure 15](#)~~Figure 15~~ and [Figure 16](#)~~Figure 16~~ show the results of the fitting procedure in the
492 case of CO. As for CO₂ the concentrations in one layer is almost independent of the surrounding layers, and the

493 information content also increase when going deeper in the atmosphere. In this example, temperature has also been
494 retrieved and is favourably compared to the temperature retrieved from CO₂ (see Figure 9.B and Figure 14.B).

495 [Figure 14](#)~~Figure-14~~

496 [Figure 15](#)~~Figure-15~~

497 [Figure 16](#)~~Figure-16~~

498 6. Conclusion

499 The present paper shows how the densities of some key constituents of the atmosphere of Venus, as well as rotational
500 temperature profiles can be retrieved from the SOIR data, using a retrieval technique based on the OE method. This
501 method allows the simultaneous derivation of the densities of all the target species, including different isotopologues .
502 The total pressure and total density profiles can also be obtained using a specific procedure, in the case of carbon dioxide
503 retrievals.

504 The error bars on the retrieved density are lower than 6%, and on the temperature are lower than 1.5%.

505 The method provides reliable vertical profiles that will be used to construct a data base of the upper Venus atmosphere at
506 the terminator, and will allow us to study the temporal and latitudinal variations of the composition of the atmosphere. A
507 CO₂ climatology is being built and will be described and discussed in the forthcoming companion paper. At the same
508 time, a detailed inventory of the composition of the atmosphere is being done in terms of CO, H₂O/HDO, HF, HCl or
509 SO₂.

510 7. Acknowledgments

511 Venus Express is a planetary mission from the European Space Agency (ESA). We wish to thank all ESA members who
512 participated in the mission, in particular H. Svedhem and O. Witasse. We thank our collaborators at IASB-
513 BIRA/Belgium, Latmos/France, and IKI/Russia. We thank CNES, CNRS, Roskosmos and the Russian Academy of
514 Science. The research program was supported by the Belgian Federal Science Policy Office and the European Space
515 Agency (ESA, PRODEX program, contracts C 90268, 90113, and 17645).

516 8. References

- 517 Altieri, F., L. Zasova, E. D'Aversa, G. Bellucci, F.G. Carrozzo, B. Gondet, and J.-P. Bibring, O₂ 1.27 μm emission
518 maps as derived from OMEGA/MEx data, *Icarus*, 204 (2), 499-511, 2009.
- 519 Belyaev, D., O. Korablev, A. Fedorova, J.-L. Bertaux, A.-C. Vandaele, F. Montmessin, A. Mahieux, V. Wilquet,
520 and R. Drummond, First observations of SO₂ above Venus' clouds by means of solar occultation in the
521 infrared, *J. Geophysical Research*, doi:10.1029/2008JE003143, 2008.
- 522 Bertaux, J.L., D. Nevejans, O. Korablev, E. Villard, E. Quémerais, E. Neefs, F. Montmessin, F. Leblanc, J.P.
523 Dubois, and E. Dimarellis, SPICAV on Venus Express: Three spectrometers to study the global structure
524 and composition of the Venus atmosphere, *Planetary and Space Science*, 55 (12), 1673-1700, 2007.

- 525 Bingen, C., F. Vanhellemont, and D. Fussen, A new regularized inversion method for the retrieval of
526 stratospheric aerosol size distributions applied to 16 years of SAGE II data (1984-2000): method, results
527 and validation, *Annales Geophysicae*, 21, 797-804, 2003.
- 528 Clancy, R.T., B. Sandor, and G.H. Moriarty-Schieven, Observational definition of the Venus mesopause: vertical
529 structure, diurnal variation, and temporal instability, *Icarus*, 161 (1), 1-16, 2003.
- 530 Clancy, R.T., B.J. Sandor, and G.H. Moriarty-Schieven, Venus Upper Atmospheric CO, Temperature, and
531 Winds across the Afternoon/Evening Terminator from June 2007 JCMT Sub-millimeter Line
532 Observations, *Planet. Space Sci.*, *accepted*, 2008.
- 533 de Bergh, C., V.I. Moroz, F.W. Taylor, D. Crisp, B. Bézard, and L.V. Zasova, The composition of the atmosphere
534 of Venus below 100 km altitude: An overview, *Planetary and Space Science*, 54 (13-14), 1389-1397, 2006.
- 535 Esposito, L.W., The clouds and hazes on Venus, in *Venus*, edited by D.M. Hunten, L. Colin, T.M. Donahue, and
536 V.I. Moroz, pp. 484-564, Univ. of arizona, 1983.
- 537 Fedorova, A., O. Korablev, A.C. Vandaele, J.-L. Bertaux, D. Belyaev, A. Mahieux, E. Neefs, V. Wilquet, R.
538 Drummond, F. Montmessin, and E. Villard, HDO and H₂O vertical distribution and isotopic ratio in the
539 Venus mesosphere by SOIR spectrometer on board Venus Express, *J. Geophys. Res.*
540 doi:10.1029/2008JE003146, 2008.
- 541 Gallery, W.O., F.X. Kneizys, and S.A. Clough, Air mass computer program for atmospheric
542 transmittance/radiance calculation: FSCATM, edited by H.A. Air Force Geophysical Laboratory, MA,
543 1983.
- 544 Gilli, G., M.A. Lopez-Valverde, P. Drossart, G. Piccioni, S. Erard, and A. Cardesin-Moinelo, Limb observations
545 of CO₂ and CO non-LTE emissions in the Venus atmosphere by VIRTIS/Venus Express, *J. Geophys.*
546 *Res.* 114 (E00B29), doi:10.1029/2008JE003112, 2009.
- 547 Hedin, A.E., H.B. Niemann, and W.T. Kasprzak, Global empirical model of the Venus thermosphere, *J. Geophys.*
548 *Res.* 88 (A1), 73-83, 1983.
- 549 Lane, W.A., and R. Opstbaum, High altitude Venus haze from Pioneer Venus limb scans, *Icarus*, 54 (1), 48-58,
550 1983.
- 551 Lopez-Valverde, M.A., Private communication.
- 552 Mahieux, A., S. Berkenbosch, R. Clairquin, D. Fussen, N. Matshvili, E. Neefs, D. Nevejans, B. Ristic, A.C.
553 Vandaele, V. Wilquet, D. Belyaev, A. Fedorova, O. Korablev, E. Villard, F. Montmessin, and J.-L.
554 Bertaux, In-Flight performance and calibration of SPICAV SOIR on board Venus Express, *Applied*
555 *Optics*, 47 (13), 2252-65, 2008.
- 556 Mahieux, A., A.C. Vandaele, V. Wilquet, S. Robert, R. Drummond, A. Fedorova, and J.L. Bertaux, Densities and
557 temperatures in the Venus mesosphere and lower thermosphere retrieved from SOIR on board Venus
558 Express. Part II. CO₂ densities and temperatures, *J. Geophys. Res.* (*in preparation*), 2010.
- 559 Mahieux, A., V. Wilquet, R. Drummond, D. Belyaev, A. Fedorova, and A.C. Vandaele, A New Method for
560 Determining the transfer function of an Acousto Optical Tunable Filter., *Optics Express*, 17, 2005-2014,
561 2009.
- 562 Mueller-Wodarg, I., and S. Tingle, Vertical structure above the clouds: towards a unified model, in *XLIII*
563 *Rencontres de Moriond, Venus Express Scientific Workshop*, La Thuile, Italy, 03-07 March, 2008.
- 564 NAIF, The SPICE Toolkit, edited by NAIF, NASA, 2009.
- 565 Nevejans, D., E. Neefs, E. Van Ransbeeck, S. Berkenbosch, R. Clairquin, L. De Vos, W. Moelans, S. Glorieux, A.
566 Baeke, O. Korablev, I. Vinogradov, Y. Kalinnikov, B. Bach, J.-P. Dubois, and E. Villard, Compact high-
567 resolution space-borne echelle grating spectrometer with AOTF based on order sorting for the infrared
568 domain from 2.2 to 4.3 micrometer, *Applied Optics*, 45 (21), 5191-5206, 2006.
- 569 Rodgers, C.D., *Inverse methods for atmospheric sounding: Theory and practice*, University of Oxford, 2000.
- 570 Rodgers, D., Characterization and Error Analysis of Profiles Retrieved From Remote Sounding Measurements, *J*
571 *. Geophys. Res.* 95 (D5), 5587-5595, 1990.
- 572 Rothman, L.S., I.E. Gordon, A. Barbe, D. Benner, P. Bernath, M. Birk, V. Boudon, L.R. Brown, A. Campargue,
573 J.-P. Champion, K. Chance, L.H. Coudert, V. Dana, V. Devi, S. Fally, J.-M. Flaud, R. Gamache, A.
574 Goldman, D. Jacquemart, I. Kleiner, N. Lacome, W. Lafferty, J.-Y. Mandin, S. Massie, S. Mikhailenko,
575 C. Miller, N. Moazzen-Ahmadi, O. Naumenko, A. Nikitin, J. Orphal, V. Perevalov, A. Perrin, A. Predoi-
576 Cross, C.P. Rinsland, M. Rotger, M. Simeckova, M.A.H. Smith, K. Sung, S. Tashkun, J. Tennyson, R.A.
577 Toth, A.C. Vandaele, and J. Vander Auwera, The HITRAN 2008 molecular spectroscopic database, *J.*
578 *Quant. Spectrosc. Radiat. Transfer*, 110 (9-10), 533-572, 2009.
- 579 Russel, J.M., and S.R. Drayson, The inference of atmospheric ozone using satellite horizon measurements in the
580 1042 cm⁻¹ band, *Journal of Atmospheric Science*, 29 (376), 1972.
- 581 Sandor, B.J., and R.T. Clancy, Water vapor variations in the Venus mesosphere from microwave spectra, *Icarus*,
582 177, 129-143, 2005.
- 583 Schroeder, D.J., and R.L. Hilliard, Echelle efficiencies: theory and experiment, *Applied Optics*, 19 (16), 2833-2841,
584 1980.
- 585 Seiff, A., J.T. Schofield, A. Kliore, F.W. Taylor, S.S. Limaye, H.E. Revercomb, L.A. Sromovsky, V.V.
586 Kerzhanovich, V.I. Moroz, and M.Y. Marov, Models of the structure of the atmosphere of Venus from
587 the surface to 100 kilometers altitude, *Adv. Space Res.*, 5 (11), 3-58, 1985.

588 Svedhem, H., D. Titov, D. McCoy, J.-P. Lebreton, S. Barabash, J.-L. Bertaux, P. Drossart, V. Formisano, B.
589 Hausler, O. Korablev, W.J. Markiewicz, D. Nevejans, M. Patzold, G. Piccioni, T.L. Zhang, F.W. Taylor,
590 E. Lellouch, D. Koschny, O. Witasse, H. Eggel, M. Warhaut, A. Accomazzo, J. Rodriguez-Canabal, J.
591 Fabrega, T. Shirmann, A. Clochet, and M. Coradini, Venus Express: The first European mission to
592 Venus, *Planet. Space Sci.*, 55 (12), 1636-1652, 2007.
593 Titov, D.V., and e. al., Venus Express science planning, *Planetary and Space Science*, 54 (13-14), 1279-1297, 2006.
594 Vandaele, A.C., M. De Mazière, R. Drummond, A. Mahieux, E. Neefs, V. Wilquet, D. Belyaev, A. Fedorova, O.
595 Korablev, F. Montmessin, and J.-L. Bertaux, Composition of the Venus mesosphere measured by SOIR
596 on board Venus Express, *J. Geophys. Res.*, doi:10.1029/2008JE003140, 2008.
597 Vandaele, A.C., M. Kruglanski, and M. De Mazière, Simulation and retrieval of atmospheric spectra using
598 ASIMUT, in *ESA Atmospheric Science Conference*, Frascati, Italy, 2006.
599 Vander Auwera, J., Private communication.
600 Wilquet, V., A. Fedorova, F. Montmessin, R. Drummond, A. Mahieux, A.C. Vandaele, E. Villard, O. Korablev,
601 and J.-L. Bertaux, Preliminary characterization of the upper haze by SPICAV/SOIR solar occultation in
602 UV to mid-IR onboard Venus Express, *J. Geophys. Res.* 114 (E00B42), doi:10.1029/2008JE003186, 2009.
603 Wilquet, V., A.C. Vandaele, A. Mahieux, S. Robert, F. Montmessin, and J.L. Bertaux, Aerosol characterization
604 and climatology observed by the SOIR instrument on board Venus Express, *Icarus*, (*In preparation*), 2010.
605
606

607 9. Table Captions

608 Table 1: Summary of pixel rows combinations.

609

610 [Table 2](#)[Table 2](#): Details of the orbit 341.1 (28/03/2007), summarizing the local UTC time, the tangent altitude, the
611 latitude and longitude of the tangent point, the pointing angle as defined in [Figure 2](#)[Figure 2](#), the distance
612 between the surface of Venus and Venus Express and the height of the projected slit at the tangent point.

613

614 10. Figure Captions

615 [Figure 1](#)[Figure 1](#): Onion peeling definition while performing a solar occultation. The tangent altitude of each
616 measurement defines a layer. The layers are spherical, and the atmospheric parameters such as the temperature
617 T_i , pressure p_i , partial pressure of a given species are considered to be constant within each layer i . The light path
618 length within layer i of the measurement j – having its tangent altitude in layer j – is denoted Δs_i^j .

619

620 [Figure 2](#)[Figure 2](#): Pointing angles and distances definition. The distance between Venus' surface and VEX is R_{VV} .
621 The tangent altitude is H_{tg} . The angle between the boresight of SOIR and the line linking the centre of Venus and
622 VEX is denoted α . The SOIR instrument is pointing 10° above the centre of the Sun to ensure that the diffracted
623 Sun remains within the slit for longer during the occultation [*Mahieux et al.*, 2008].

624

625 [Figure 3](#)[Figure 3](#): Representation of the slit. The slit has a width of $30'$ and a height of $2'$. In the binning
626 configuration 2×12 pixel rows, it is divided in 2 groups. The axes depicted are the ones used by the Spice routine.
627 The slit is tilted by an angle γ . The Sun is located along the $+z$ axis. The centre of the slit is the origin of the x, y, z
628 coordinates.

629

630 [Figure 4](#)[Figure 4](#)Error! Reference source not found.: Procedure to simulate a SOIR spectrum. Panel A shows the
631 absorption cross section of CO_2 around 3340 cm^{-1} . It has been calculated for one layer with atmospheric
632 conditions at 90 km. Panel B shows the transmittance T of these lines, after using the Beer-Lambert law. Panel C
633 is the transmittance T after convolution by the instrument function. Panel D is the spectrum multiplied by the
634 AOTF transfer function. The different diffraction orders are also indicated. The order overlap is clearly seen.
635 Panel E shows the contribution of the different orders: the bold line is the central order 149, the dashed line is the

636 order +1 and the dash-dotted line is the order -1. Panel F shows the sum of the contribution of the three
637 considered orders. One can see that the role of the adjacent orders cannot be neglected, as absorption features of
638 the adjacent order may have significant contributions.

639

640 **Figure 5**: Determination of the altitude range. The altitude range is determined by studying the quotient
641 I_{mean}/I_{diff} , with I_{mean} being mean value of the spectrum on the interval fitted, and I_{diff} being the maximum less
642 the minimum value on the interval. The figure presented on Panel C depicts its variation as a function of altitude.
643 At high altitude, above point 1 – see spectrum in Panel A, I_{mean}/I_{diff} is a majoring value of the noise level. When
644 the absorption structures start appearing the spectra, at point 2 – see spectrum in Panel B, an inflection point is
645 observed in the curve. It is observed that the second inflection point – point 3 – corresponds to the altitude when
646 the absorption lines are completely saturated.

647

648 **Figure 6**: Temperature dependency. This Figure shows that the temperature information is influenced by
649 the shape of the AOTF transfer function. The top panel is a CO₂ spectrum in diffraction order 149, simulated for
650 a layer (atmospheric conditions: altitude of 110 km, pressure of 0.152 Pa, temperature of 181.2 K, total density of
651 $0.1 \times 10^{-4} \text{ mol/m}^3$, volume mixing ratio of 0.965, path length of 200 km), but without order addition nor
652 contribution of the AOTF transfer function. It is clearly seen that the maximum of absorption of the band is
653 located around 3347 cm^{-1} . The bottom panel shows the measured spectrum, and the shape of the AOTF function.
654 It is obvious that the maximum of the measured transmittance has been displaced closer to the maximum of the
655 AOTF transfer function.

656

657 **Figure 7**: Spectra measured during orbit 341.1 (28/03/2007). The selected orders were 112 (Panel A), 130
658 (Panel B), 149 (Panel C) and 190 (Panel D). Each Panel depicts all the spectra taken during the occultation in the
659 selected diffraction order. The absorption features observed in Panel A come from $^{16}\text{O}^{12}\text{C}^{18}\text{O}$, in Panel B from
660 $^1\text{H}^{15}\text{Cl}$ and $^1\text{H}^{35}\text{Cl}$, in Panel C from $^{16}\text{O}^{12}\text{C}^{16}\text{O}$ and in Panel D from $^{12}\text{C}^{16}\text{O}$.

661

662 **Figure 8**: Trace of the measurement points of diffraction order 149 on a local solar time vs. latitude map.
663 The measurements occur either at 6:00 AM or 6:00 PM, on the morning or the evening terminators. A gap is seen
664 at the morning terminator between 50° and 60° north, as well as on the evening terminator between 35° and 70°
665 north. This is due to the orbit geometry, implying that few solar occultations occur for VEX at these latitudes.

666

Formatted:

667 | [Figure 9](#)**Figure 9:** Vertical profiles obtained from the retrieval of the orbit 341, using order 149: CO₂ density in
668 | Panel A, temperature in Panel B, wavenumber shift in Panel C, aerosols parameters in Panels D, E and F .
669 | Reference vertical profiles (dashed), from the combination of the VIRA model [*Seiff et al.*, 1985] and the VTS3
670 | model [*Hedin et al.*, 1983]; retrieved profile (plain). The errors obtained from the Optimal Estimation algorithm
671 | are also plotted on the graphs.

672

673 | [Figure 10](#)**Figure 10:** Illustration of the quality of the spectral fit obtained during the CO₂ retrieval of orbit 341,
674 | order 149. For each altitude, the Top Panel compares the observed (blue) and fitted (green) transmittances, and
675 | the Bottom Panel illustrates the residuals (observed - fitted transmittances). Also in the Top Panel, red represents
676 | the calculated transmittance outside the fitting wavenumber range.

677

678 | [Figure 11](#)**Figure 11:** Averaging kernels of the last step of the Optimal Estimation algorithm from the retrieval of
679 | CO₂ of orbit 341, order 149: (a) aerosols a parameter; (b) aerosols b parameter; (c) CO₂ vertical densities; (d)
680 | rotational temperature vertical profile and (e) wavenumber shift. The averaging kernels show the area of
681 | dependency of each variable.

682

683 | [Figure 12](#)**Figure 12:** CO₂ vertical profiles coming from three different diffraction orders, allowing covering a
684 | wider vertical altitude range. They were obtained from the orbits 1119.1 (14/05/2009, 80.4°N, 06:30PM), 1221.1
685 | (16/05/2009, 83.1°N, 06:48PM), 1125.1(20/05/2009, 84.6° N, 07:12PM) and 1133.1 (28/05/2009, 87.6°N, 10:00PM).

686

687 | [Figure 13](#)**Figure 13:** CO₂ rotational temperature vertical profiles coming from three different diffraction orders,
688 | allowing covering a wider vertical altitude range. They were obtained from the orbits 1119.1 (14/05/2009, 80.4°N,
689 | 06:30PM), 1221.1 (16/05/2009, 83.1°N, 06:48PM), 1125.1(20/05/2009, 84.6° N, 07:12PM) and 1133.1 (28/05/2009,
690 | 87.6°N, 10:00PM).

691

692 | [Figure 14](#)**Figure 14:** Vertical profiles – (A) CO density, (B) temperature, (C) wavenumber shift and (D, E, F)
693 | aerosols parameters– obtained from the retrieval of the orbit 341, using order 190 : retrieved profile (plain) ;
694 | reference vertical profiles (dashed), combination of the VIRA model [*Seiff et al.*, 1985] and the VTS33 model
695 | [*Hedin et al.*, 1983]. The temperature is the one retrieved during the CO₂ retrieval. The errors obtained from the
696 | Optimal Estimation algorithm are also plotted on the graphs

697

698 | **Figure 15** ~~Figure 15~~: Illustration of the quality of the spectral fit obtained during the CO retrieval of orbit 341,
699 | order 190. For each altitude, the Top Panel compares the observed (blue) and fitted (green) transmittances, and
700 | the Bottom Panel illustrates the residuals (observed - fitted transmittances). Also in the Top Panel, red represents
701 | the calculated transmittance outside the fitting wavenumber range.

702

703 | **Figure 16** ~~Figure 16~~: Averaging kernels of the last step of the Optimal Estimation algorithm from the retrieval of
704 | CO of orbit 341, order 190: (a) aerosols a parameter; (b) aerosols b parameter; (c) CO vertical densities; (d)
705 | rotational temperature profile. The averaging kernels show the area of dependency of each variable.

706

707

Denomination	Number of scanned orders per second	Number of lines in each group	Number of lines groups
2 x 16	4	16	2
2 x 12	4	12	2
4 x 4	2	4	4
4 x 3	2	3	4
8 x 4	1	4	8
8 x 3	1	3	8

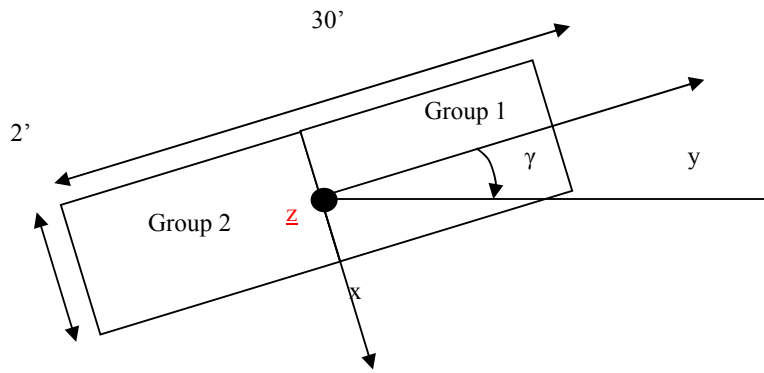
708 **Table 1**

709

UTC time	Tangent altitude [km]	Latitude [°]	Longitude [°]	Pointing angle [°]	Distance to surface [km]	Height of the projected slit [km]
2007-03-28T06:25:45.880	120.0	82.7	349.2	117.9	934.0	2.0
2007-03-28T06:25:44.880	118.3	82.7	349.2	118.0	936.6	2.0
2007-03-28T06:25:43.880	116.6	82.7	349.2	118.1	939.2	2.0
2007-03-28T06:25:42.880	114.8	82.7	349.1	118.1	941.8	2.0
2007-03-28T06:25:41.880	113.1	82.6	349.1	118.2	944.4	2.0
2007-03-28T06:25:40.880	111.4	82.6	349.0	118.3	947.0	2.0
2007-03-28T06:25:39.880	109.7	82.6	349.0	118.4	949.6	2.0
2007-03-28T06:25:38.880	107.9	82.6	349.0	118.4	952.2	2.0
2007-03-28T06:25:37.880	106.2	82.6	348.9	118.5	954.8	2.1
2007-03-28T06:25:36.880	104.5	82.5	348.9	118.6	957.5	2.1
2007-03-28T06:25:35.880	102.7	82.5	348.9	118.6	960.1	2.1

710 **Table 2**

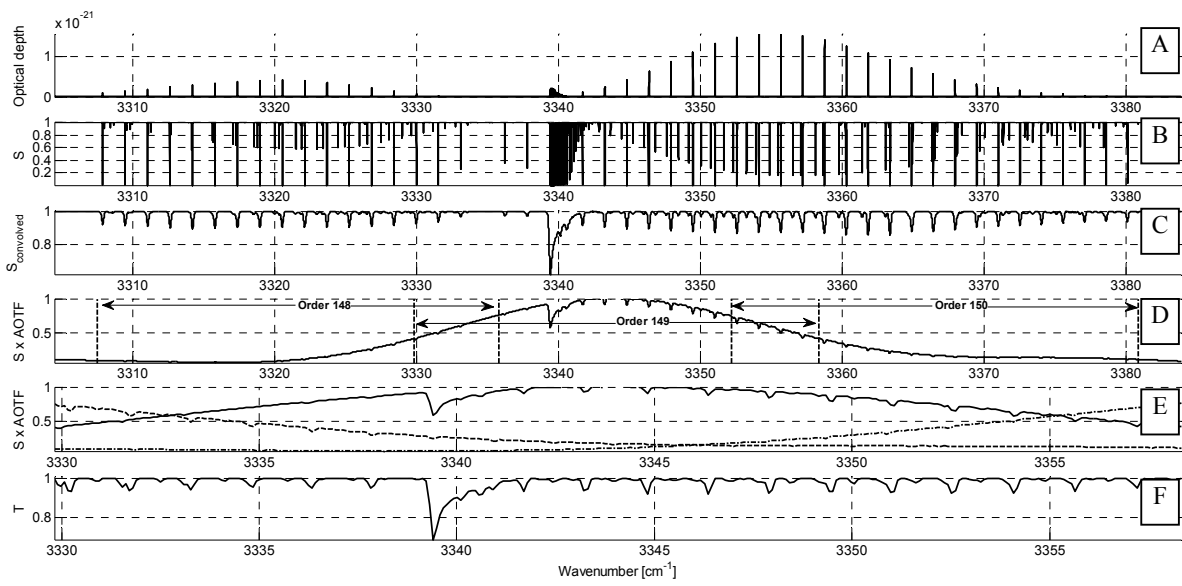
711



723

724 **Figure 3**

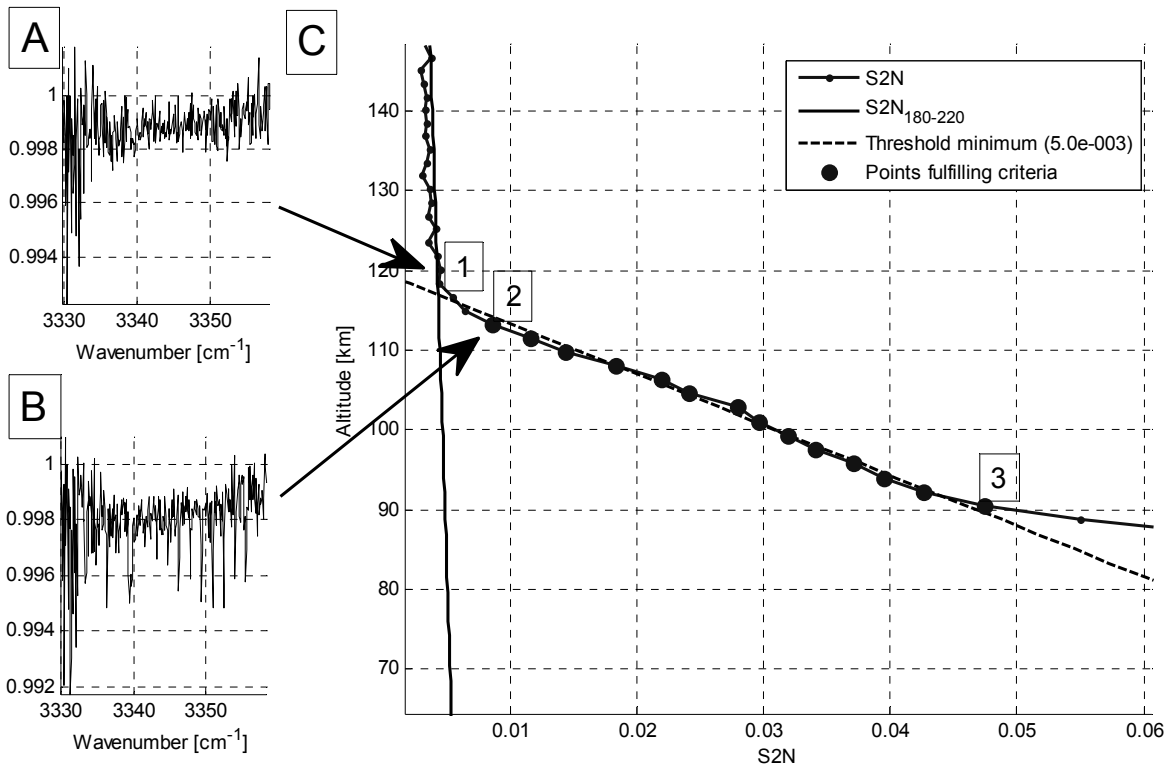
725



726

727 **Figure 4**

728



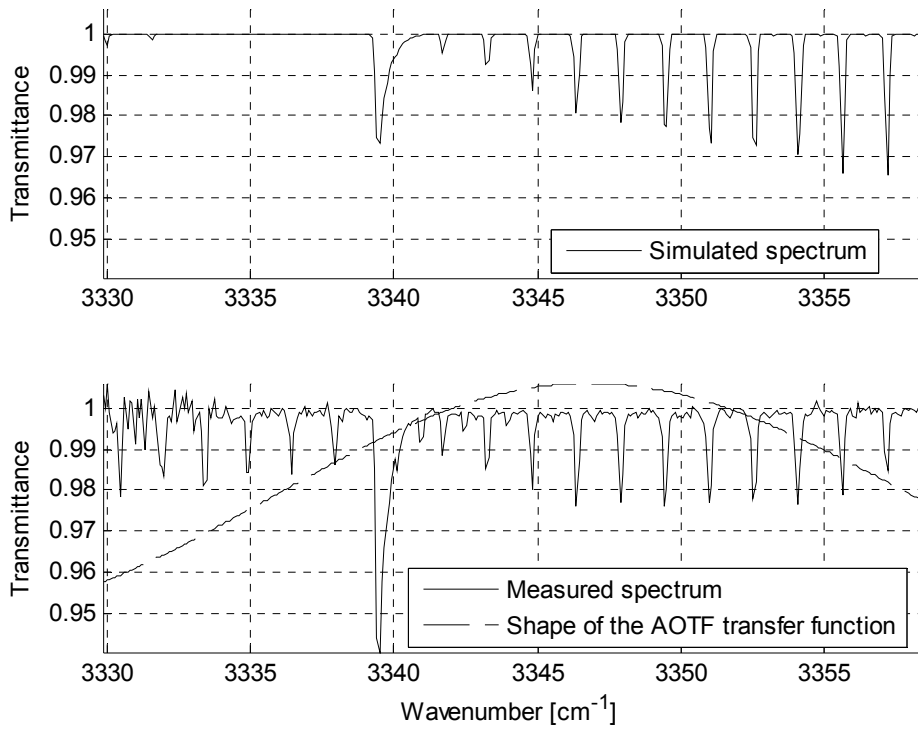
729

730 **Figure 5**

731

732

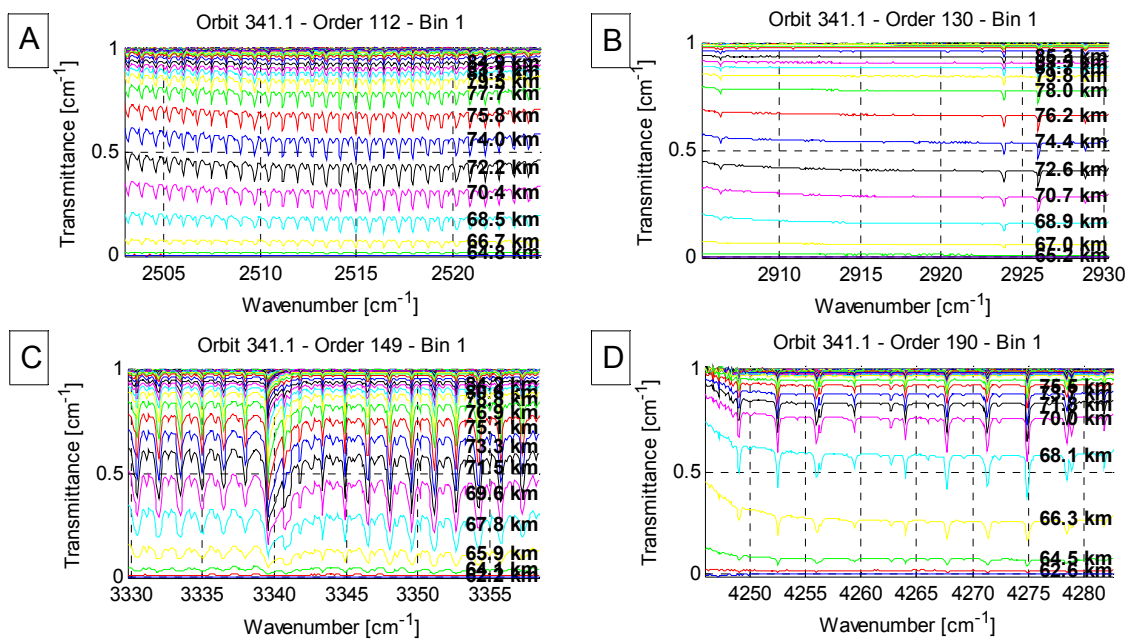
733



734

735 **Figure 6**

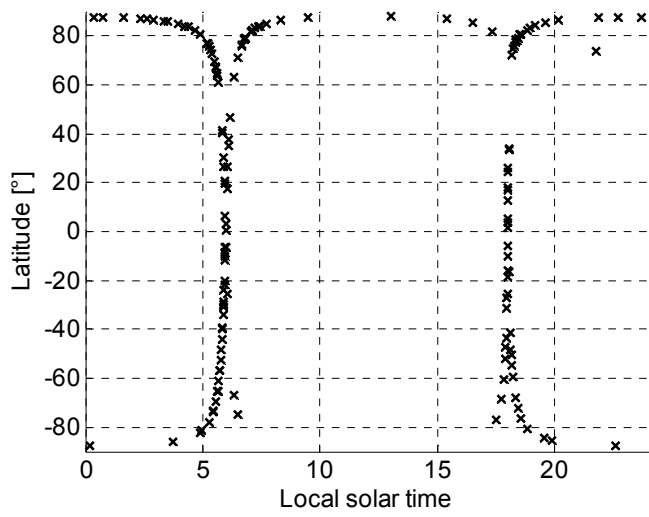
736



737

738 **Figure 7**

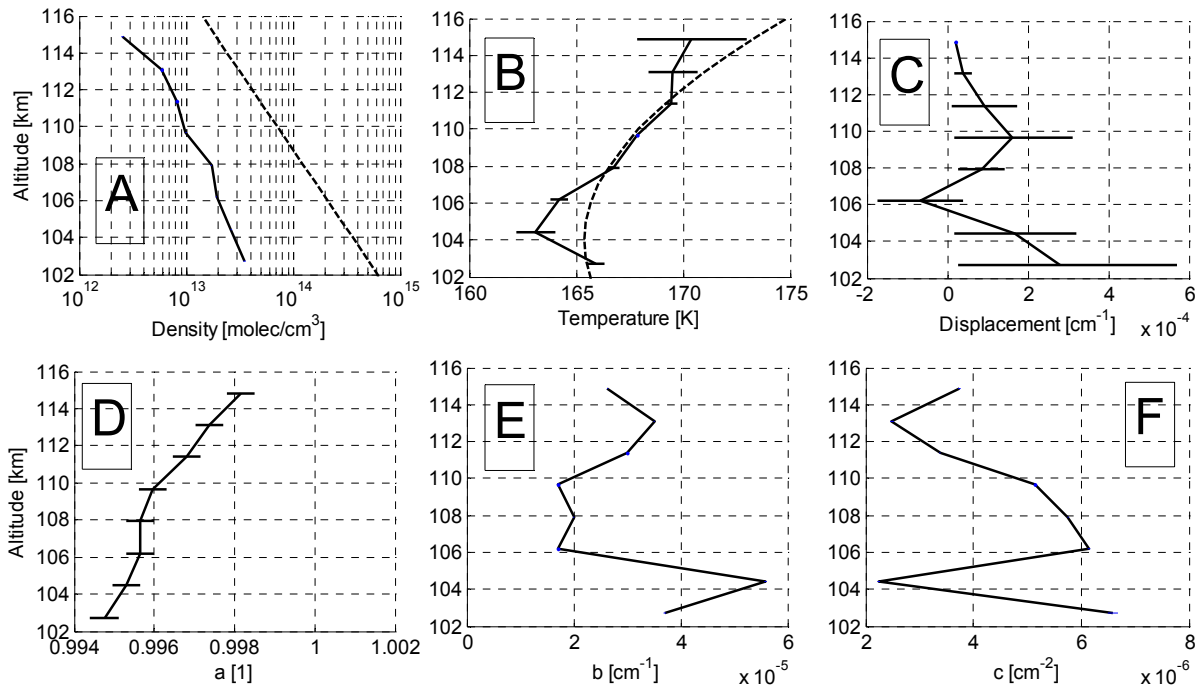
739



740

741 **Figure 8**

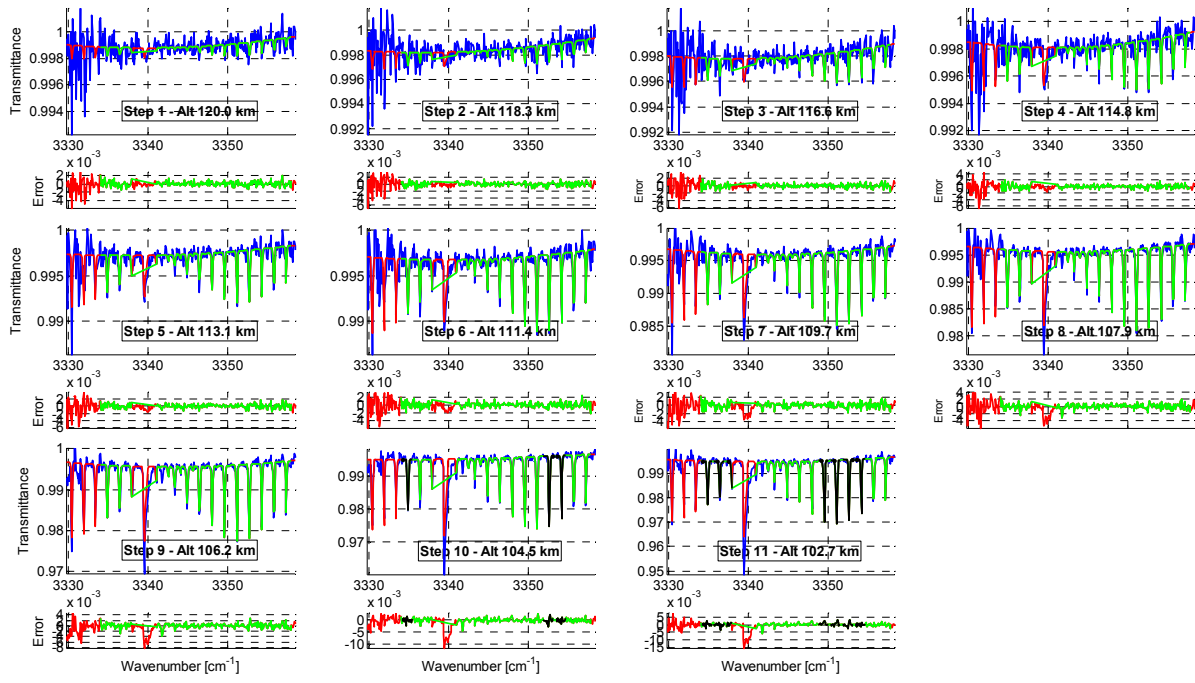
742



743

744 **Figure 9**

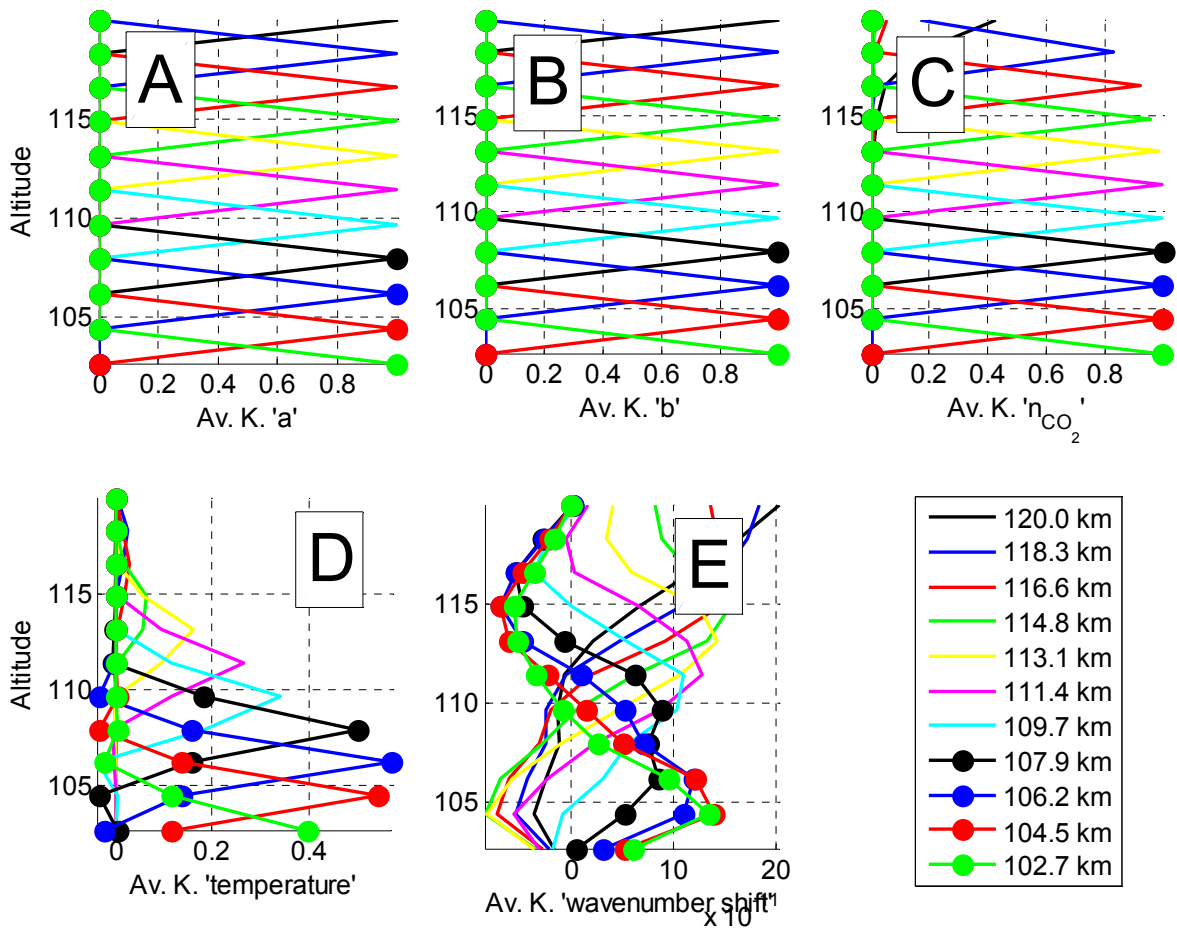
745



746

747 **Figure 10**

748

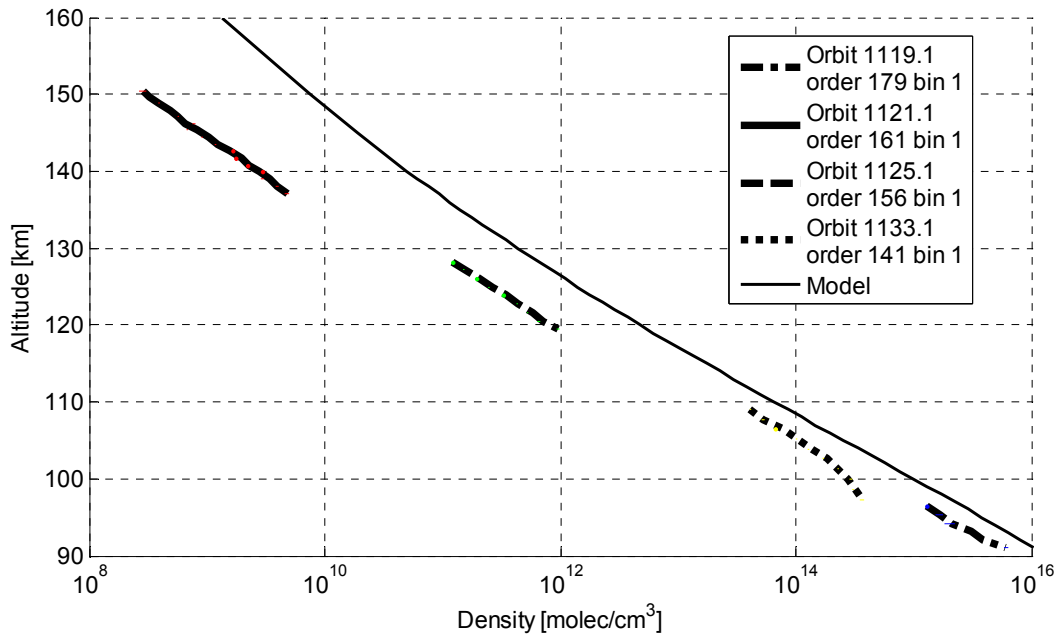


749

750 **Figure 11**

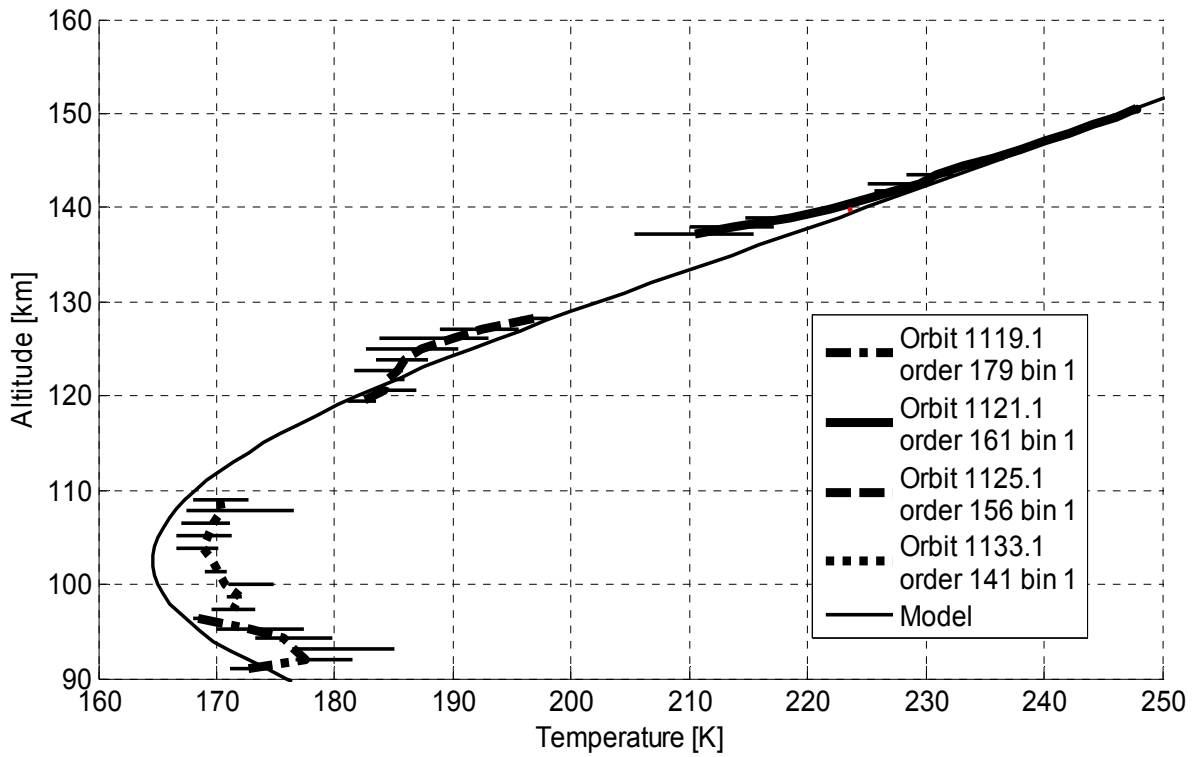
751

752



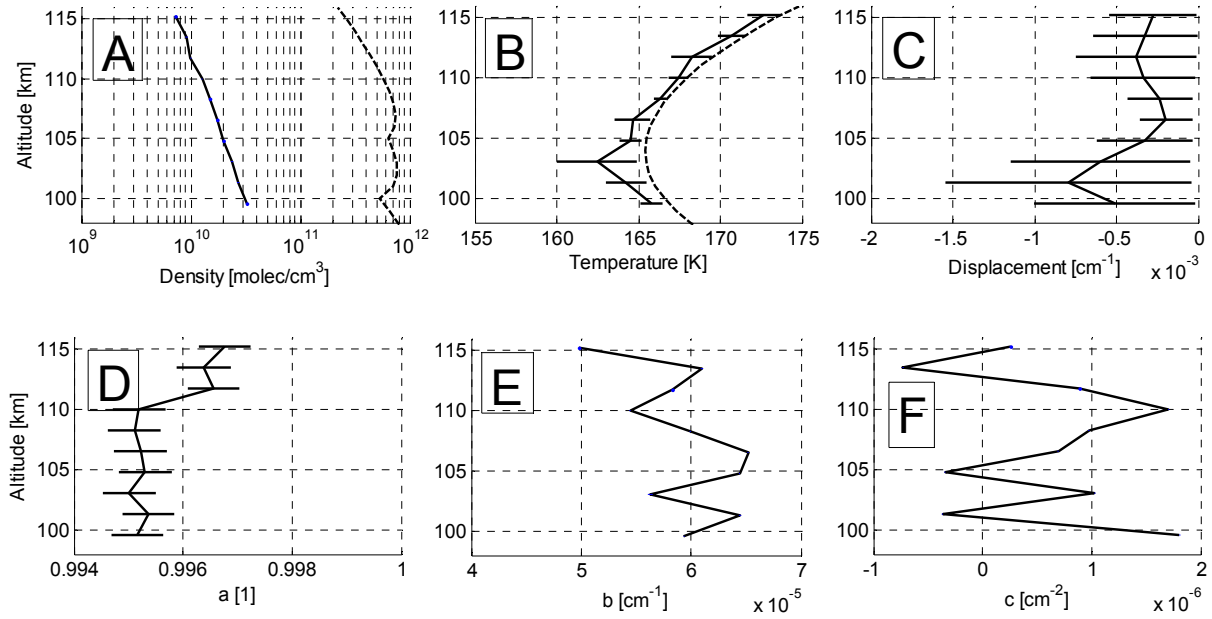
753

754 **Figure 12**



755

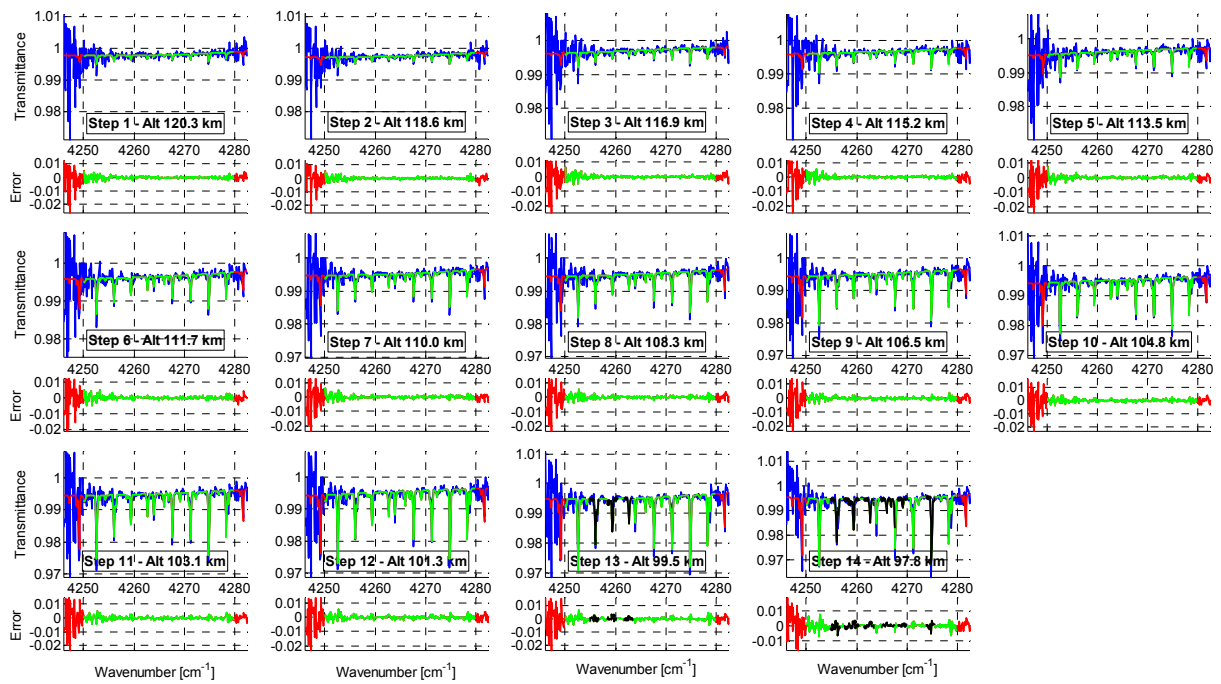
756 **Figure 13**



758

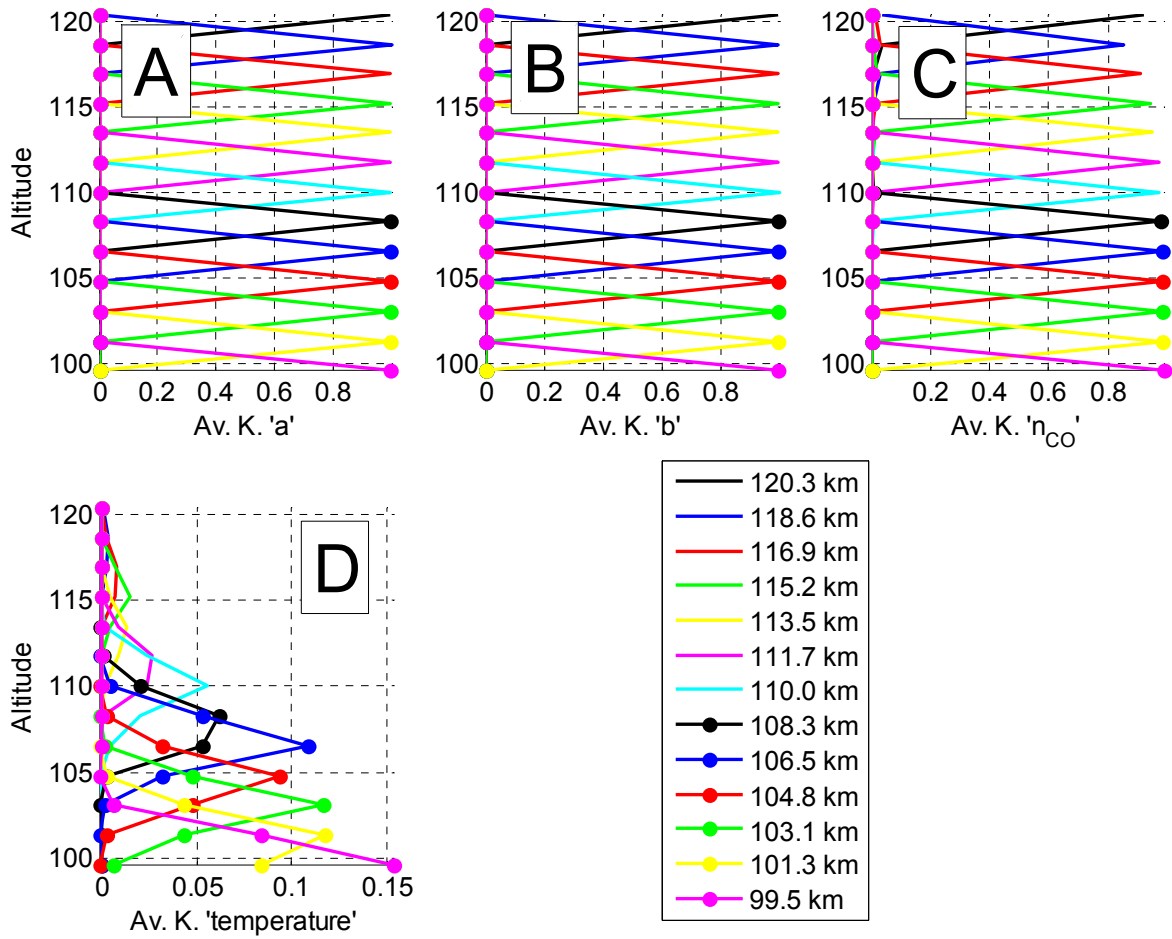
759 **Figure 14**

760



761

762 **Figure 15**



764

765 **Figure 16**

766

767

768